

# Nonlinear hydrodynamical evolution of rotating relativistic stars: Numerical methods and code tests

José A. Font<sup>1</sup>, Nikolaos Stergioulas<sup>1,2</sup> and Kostas D. Kokkotas<sup>2</sup>

<sup>1</sup>*Max-Planck-Institut für Gravitationsphysik  
Albert-Einstein-Institut  
Am Mühlenberg 5, D-14476, Golm, Germany*

<sup>2</sup>*Department of Physics  
Aristotle University of Thessaloniki  
Thessaloniki 54006, Greece*

## ABSTRACT

We present numerical hydrodynamical evolutions of rapidly rotating relativistic stars, using an axisymmetric, nonlinear relativistic hydrodynamics code. We use four different high-resolution shock-capturing (HRSC) finite-difference schemes (based on approximate Riemann solvers) and compare their accuracy in preserving uniformly rotating stationary initial configurations in long-term evolutions. Among these four schemes, we find that the third-order PPM scheme is superior in maintaining the initial rotation law in long-term evolutions, especially near the surface of the star. It is further shown that HRSC schemes are suitable for the evolution of perturbed neutron stars and for the accurate identification (via Fourier transforms) of normal modes of oscillation. This is demonstrated for radial and quadrupolar pulsations in the nonrotating limit, where we find good agreement with frequencies obtained with a linear perturbation code. The code can be used for studying small-amplitude or nonlinear pulsations of differentially rotating neutron stars, while our present results serve as testbed computations for three-dimensional general-relativistic evolution codes.

**Key words:** Hydrodynamics — relativity — methods: numerical — stars: neutron — stars: oscillations — stars: rotation

## 1 INTRODUCTION

The hydrodynamical evolution of neutron stars in numerical relativity has been the focus of many research groups in recent years (see e.g. Font et al. 1999; Miller, Suen & Tobias 1999; Mathews, Marronetti & Wilson 1998; Shibata 1999a, Nakamura & Oohara 1998; Baumgarte, Hughes & Shapiro 1999; Neilsen & Choptuik 1999). So far, these studies have been limited to initially non-rotating stars<sup>\*</sup>. However, the numerical investigation of many interesting astrophysical applications, such as the rotational evolution of proto-neutron

stars and merged neutron stars or the simulation of gravitational radiation from unstable pulsation modes, requires the ability of accurate long-term evolutions of rapidly rotating stars. We thus present here an extensive investigation of the nonlinear hydrodynamical evolution of rotating neutron stars (first results of this study were presented in Stergioulas, Font & Kokkotas 1999). As we focus on the implementation and problems of the hydrodynamical evolution of initially stationary configurations in stable equilibrium, we do not evolve the spacetime. This approximation allows us to evolve relativistic matter for a much longer time than present coupled spacetime plus hydrodynamical evolution codes. When studying the evolution of perturbed rotating neutron stars, the approximation of a static spacetime still allows for qualitative conclusions to be

<sup>\*</sup> After this work was completed, we received a preprint by Shibata 1999b, in which evolutions of approximate solutions of rotating stars are shown.

drawn, since pulsations of neutron stars are mainly a hydrodynamical process.

The rotational evolution of neutron stars can be affected by several instabilities (see Stergioulas 1998 for a recent review). If hot proto-neutron stars are rapidly rotating, they can undergo a dynamical bar-mode instability (Houser, Centrella & Smith 1994). When the neutron star has cooled to about  $10^{10}$  K after its formation, it can be subject to the Chandrasekhar-Friedman-Schutz instability (Chandrasekhar 1970; Friedman & Schutz 1978) and it becomes an important source of gravitational waves. It was recently found that the  $l = m = 2$   $r$ -mode has the shortest growth time of the instability (Andersson 1998; Friedman & Morsink 1998) and it can transform a rapidly rotating newly-born neutron star to a Crab-like slowly-rotating pulsar within about a year after its formation (Andersson, Kokkotas & Schutz 1999; Lindblom, Owen & Morsink 1998). In this model, there are several important questions still to be answered: What is the maximum amplitude that an unstable  $r$ -mode can reach (limited by nonlinear saturation)? Is there significant transfer of energy to other stable or unstable modes via nonlinear couplings? (Owen et al. 1998). Does the  $r$ -mode evolution in a uniformly rotating star lead to differential rotation? (Spruit 1999, Rezzolla et al. 1999, Friedman 1999). Such questions cannot be answered by computations of normal modes of the linearized pulsation equations, but require nonlinear effects to be taken into account. In addition, the computation of the frequency of  $r$ -modes in a rapidly rotating relativistic star may be easier to achieve in nonlinear numerical evolutions than in a perturbative computation. It is therefore desirable to develop the capability of full nonlinear numerical evolutions of rotating stars in relativity. The present implementation of the hydrodynamical evolution is a first step in this direction.

For our study we have developed an axisymmetric numerical code in spherical polar coordinates which uses high-resolution shock-capturing (HRSC) finite-difference schemes for the numerical integration of the general relativistic hydrodynamic equations (see Ibáñez & Martí 1999 for a recent review of applications of HRSC schemes in relativistic hydrodynamics). Such schemes have been successfully used before, in the study of the numerical evolution and gravitational collapse of nonrotating neutron stars in 1-D (Romero et al. 1996). An alternative approach, based on pseudospectral methods, has been presented by Gourgoulhon (1991). Using our code in 1-D, we can accurately identify radial normal modes of pulsation up to high harmonic order. In 2-D the code is suitable for the hydrodynamical evolution of rotating stars and the study of axisymmetric modes of pulsation.

We find that the evolution of rotating stars with HRSC schemes can be subject to a significant numerical difficulty at the surface of the star. This difficulty

arises due to the fact that one of the evolved hydrodynamical variables, which corresponds to the angular momentum, has a sharp discontinuity at the surface. The result of a time-dependent evolution is a secular drift of the evolved configuration from the initial rotation law, near the surface. We investigate this problem, using two different classes of HRSC schemes: Total Variation Diminishing (TVD, Harten 1984) and Essentially Non-Oscillatory (ENO, Harten & Osher 1987; Harten et al. 1987). We use both second and third-order variations of these schemes and find that, for a given resolution, the third-order schemes are superior in dealing with this problem. In addition, we show that all schemes are suitable for identifying normal modes of pulsation in a hydrodynamical evolution, via Fourier transforms of the evolved variables.

In a subsequent paper we will present frequencies of quasi-radial and axisymmetric pulsations of rapidly rotating neutron stars. We further plan to study the pulsations of differentially rotating, hot proto-neutron stars and determine possible nonlinear couplings of different modes of pulsation.

The paper is organized as follows: In Section 2 we describe the initial equilibrium configurations which will be evolved with the hydrodynamical code. In Section 3, we present the explicit form of the equations of general relativistic hydrodynamics as implemented in our code. Section 4 is devoted to the description of the numerical implementation of the evolution schemes. Finally, Section 5 presents 1-D and 2-D tests of the code with the various implemented schemes.

## 2 INITIAL CONFIGURATIONS

Our initial models are exact numerical solutions of rapidly rotating relativistic stars, having uniform angular velocity  $\Omega$ . The metric of the stationary and axisymmetric spacetime in quasi-isotropic coordinates is

$$ds^2 = -e^{2\nu} dt^2 + B^2 e^{-2\nu} r^2 \sin^2 \theta (d\phi - \omega dt)^2 + e^{2\alpha} (dr^2 + r^2 d\theta^2), \quad (1)$$

where  $\nu$ ,  $B$ ,  $\alpha$  and  $\omega$  are metric functions (Butterworth & Ipser 1976). In the non-rotating limit the above metric reduces to the metric of spherical relativistic stars in isotropic coordinates. We use dimensionless quantities by setting  $c = G = M_\odot = 1$ .

We assume a perfect fluid, zero-temperature equation of state (EOS), for which the energy density is a function of pressure only. The following relativistic generalization of the Newtonian polytropic EOS is chosen:

$$p = K \rho_0^{1+1/N} \quad (2)$$

$$\epsilon = \rho_0 + Np, \quad (3)$$

where  $p$  is the pressure,  $\epsilon$  is the energy density,  $\rho_0$  is the rest-mass density,  $K$  is the polytropic constant and  $N$  is the polytropic exponent. This form of a relativistic

polytropic EOS is convenient to use, since it coincides with the ideal fluid EOS used in many relativistic hydrodynamical codes, in the case of an adiabatic evolution.

The initial equilibrium models are computed using a numerical code by Stergioulas & Friedman (1995) which follows the Komatsu, Eriguchi & Hachisu (KEH, 1989) method (as modified in Cook, Shapiro & Teukolsky, CST, 1992) with some changes for improved accuracy. In the KEH method three of the four general-relativistic, partial-differential field equations are converted to integral equations using appropriate Green's functions. The boundary conditions at infinity are thus incorporated in the integral evaluation. We use a compactified coordinate (introduced by CST) that allows one to integrate over the whole spacetime. The code has been shown to be highly accurate in extensive comparisons to other numerical codes (Nozawa et al. 1998). A public domain version is available at the following URL address: <http://www.gravity.phys.uwm.edu/Code/rns>.

The initial model is supplemented by a uniform, nonrotating “atmosphere” of very low density (typically  $10^{-6}$  or less times the central density of the star). This is necessary for computing non-singular solutions of the hydrodynamic equations everywhere in the computational domain. After each time-step, we reset the density, pressure and velocity in the atmosphere to their initial values. The influence of the atmosphere is thus minimized and restricted to the grid-cells through which the surface of the star passes. The radial velocity of the atmosphere is only set to zero after each time-step, if it is negative. This avoids unwanted accretion of the material in the atmosphere onto the star and at the same time allows the star to expand, during radial pulsations.

### 3 GENERAL RELATIVISTIC HYDRODYNAMIC EQUATIONS

The equations of general relativistic hydrodynamics are obtained from the local conservation laws of density current  $J^\mu$  and stress-energy  $T^{\mu\nu}$

$$\nabla_\mu J^\mu = 0, \quad (4)$$

$$\nabla_\mu T^{\mu\nu} = 0 \quad (5)$$

with

$$J^\mu = \rho_0 u^\mu, \quad (6)$$

$$T^{\mu\nu} = \rho_0 h u^\mu u^\nu + p g^{\mu\nu}, \quad (7)$$

for a general EOS of the form  $p = p(\rho, \varepsilon)$ . Greek (Latin) indices run from 0 to 3 (1 to 3). This choice of the stress-energy tensor limits our study to perfect fluids.

In the previous expressions  $\nabla_\mu$  is the covariant derivative associated with the four-dimensional metric  $g_{\mu\nu}$ ,  $u^\mu$  is the fluid 4-velocity and  $h$  is the specific

enthalpy

$$h = 1 + \varepsilon + \frac{p}{\rho_0} \quad (8)$$

with  $\varepsilon$  being the specific internal energy, related to the energy density  $\varepsilon$  by

$$\varepsilon = \frac{\varepsilon}{\rho_0} - 1. \quad (9)$$

With an appropriate choice of matter fields the equations of relativistic hydrodynamics constitute a hyperbolic system and can be written in a flux conservative form, as was first shown by Martí, Ibáñez and Miralles (1991) for the one-dimensional case. The knowledge of the characteristic fields of the system allows the numerical integration to be performed by means of advanced HRSC schemes, using approximate Riemann solvers (Godunov-type methods). The multi-dimensional case was studied by Banyuls et al. (1997) within the framework of the 3+1 formulation. Further extensions of this work to account for *dynamical* spacetimes, described by the full set of Einstein's non-vacuum equations, can be found in Font et al. (1999). Fully *covariant* formulations of the hydrodynamic equations (i.e., not restricted to *spacelike* approaches) and also adapted to Godunov-type methods, have been recently presented by Papadopoulos and Font (1999).

In the present work we use the hydrodynamic equations as formulated in Banyuls et al. (1997). Specializing for the metric given by Eq. (1), the 3+1 quantities read

$$\tilde{\alpha} = e^\nu, \quad (10)$$

$$\beta_\phi = -\omega B^2 e^{-2\nu} r^2 \sin^2 \theta, \quad (11)$$

$$\gamma_{rr} = e^{2\alpha}, \quad (12)$$

$$\gamma_{\theta\theta} = r^2 e^{2\alpha}, \quad (13)$$

$$\gamma_{\phi\phi} = B^2 e^{-2\nu} r^2 \sin^2 \theta, \quad (14)$$

where  $\tilde{\alpha}$  is the lapse function (the tilde is used to avoid confusion with the metric potential  $\alpha$ ),  $\beta_\phi$  is the azimuthal shift and  $\gamma_{ij}$  is the 3-metric induced on each spacelike slice.

The (axisymmetric) hydrodynamic equations are written as a first-order flux conservative system of the form

$$\frac{\partial \mathbf{u}}{\partial t} + \frac{\partial \tilde{\alpha} \mathbf{f}^r}{\partial r} + \frac{\partial \tilde{\alpha} \mathbf{f}^\theta}{\partial \theta} = \mathbf{s}, \quad (15)$$

expressing the conservation of mass, momentum and energy, where  $\mathbf{u}$ ,  $\mathbf{f}^r$ ,  $\mathbf{f}^\theta$  and  $\mathbf{s}$  are, respectively, the state vector of evolved quantities, the radial and polar fluxes and the source terms. More precisely, they take the form

$$\mathbf{u} = (D, S_r, S_\theta, S_\phi, \tau), \quad (16)$$

$$\mathbf{f}^r = (Dv^r, S_r v^r + p, S_\theta v^r, S_\phi v^r, (\tau + p)v^r), \quad (17)$$

$$\mathbf{f}^\theta = (Dv^\theta, S_r v^\theta, S_\theta v^\theta + p, S_\phi v^\theta, (\tau + p)v^\theta). \quad (18)$$

The source terms can be decomposed in the following way

$$\mathbf{s} = \tilde{\alpha} \mathbf{s}^* - \tilde{\alpha} \mathbf{f}^r \frac{\partial \log \sqrt{\gamma}}{\partial r} - \tilde{\alpha} \mathbf{f}^\theta \frac{\partial \log \sqrt{\gamma}}{\partial \theta} \quad (19)$$

with  $\gamma = \det \gamma_{ij}$  and

$$\mathbf{s}^* = \left( 0, T^{\mu\nu} \left[ \frac{\partial g_{\nu j}}{\partial x^\mu} - \Gamma_{\mu\nu}^\delta g_{\delta j} \right], \right. \\ \left. \tilde{\alpha} \left[ T^{\mu t} \frac{\partial \log \tilde{\alpha}}{\partial x^\mu} - T^{\mu\nu} \Gamma_{\mu\nu}^t \right] \right) \quad (20)$$

with  $j = r, \theta, \phi$ . Quantities  $\Gamma_{\mu\nu}^\delta$  stand for the four-dimensional Christoffel symbols. The definitions of the evolved quantities in terms of the ‘‘primitive’’ variables  $\mathbf{w} = (\rho_0, v_j, \varepsilon)$  are

$$D = \rho_0 W, \quad (21)$$

$$S_j = \rho_0 h W^2 v_j, \quad (22)$$

$$\tau = \rho_0 h W^2 - p - D, \quad (23)$$

where  $W$  is the relativistic Lorentz factor

$$W \equiv \tilde{\alpha} u^t = \frac{1}{\sqrt{1 - v^2}} \quad (24)$$

with  $v^2 = \gamma_{ij} v^i v^j$ . The 3-velocity components are obtained from the spatial components of the 4-velocity in the following way

$$v^i = \frac{u^i}{W} + \frac{\beta^i}{\tilde{\alpha}}. \quad (25)$$

#### 4 NUMERICAL SCHEMES FOR THE HYDRODYNAMIC EQUATIONS

We turn now to the description of the numerical implementation of the equations presented in the previous section. As we are investigating the accuracy of the evolution of rotating neutron stars with different schemes, we include here a detailed technical description of the different numerical methods and tools we have implemented in our code. A point we emphasize is the use of high-order polynomial cell-reconstruction procedures, to achieve a better representation of the angular-momentum discontinuity at the surface of the star.

##### 4.1 A high-resolution shock-capturing algorithm

Our hydrodynamical code performs the numerical integration of system (15) using Godunov-type (HRSC) methods. In a HRSC scheme, the knowledge of the characteristic fields (eigenvalues) of the equations, together with the corresponding eigenvectors, allows for accurate integrations, by means of either exact or approximate Riemann solvers. These solvers, which constitute the kernel of our numerical algorithm, compute, at every interface of the numerical grid, the solution of

local Riemann problems (i.e., the simplest initial value problem with discontinuous initial data). Hence, HRSC schemes automatically guarantee that physical discontinuities appearing in the solution, e.g., shock waves, are treated consistently (the *shock-capturing* property). HRSC schemes are also known for giving stable and sharp discrete shock profiles and for having a high order of accuracy, typically second order or more, in smooth regions of the solution.

In our code we perform the time update of system (15) from  $t^n$  to  $t^{n+1}$  according to the following conservative algorithm:

$$\mathbf{u}_{i,j}^{n+1} = \mathbf{u}_{i,j}^n - \frac{\Delta t}{\Delta r} (\hat{\mathbf{f}}_{i+1/2,j} - \hat{\mathbf{f}}_{i-1/2,j}) \\ - \frac{\Delta t}{\Delta \theta} (\hat{\mathbf{g}}_{i,j+1/2} - \hat{\mathbf{g}}_{i,j-1/2}) \\ + \Delta t \mathbf{s}_{i,j}, \quad (26)$$

improved with the use of consecutive sub-steps to gain accuracy in time (see Shu & Osher 1989). Index  $n$  represents the time level and the time (space) discretization interval is indicated by  $\Delta t$  ( $\Delta r, \Delta \theta$ ). The ‘‘hat’’ in the fluxes denotes the so-called numerical fluxes which are computed by means of an approximate Riemann solver according to a generic flux-formula (suppressing index  $j$ ):

$$\hat{\mathbf{f}}_{i+1/2} = \frac{1}{2} (\mathbf{f}(\mathbf{u}^L) + \mathbf{f}(\mathbf{u}^R) - Q). \quad (27)$$

The flux-formula makes use of the complete characteristic information of the system, eigenvalues (characteristic speeds) and right and left eigenvectors through the *viscosity term*  $Q$ . This information is used to provide the appropriate amount of numerical dissipation to obtain accurate representations of discontinuous solutions without excessive smearing, avoiding, at the same time, the growth of spurious numerical oscillations associated with the Gibbs phenomenon. Generic expressions for the characteristic speeds and right eigenvectors for the general relativistic hydrodynamic equations can be found in Font et al (1999). The left eigenvectors have been obtained by Ibáñez (1998).

Notice that the numerical flux is computed at the cell interfaces (e.g.,  $i \pm 1/2$ ) using information from the left and right sides. The state variables,  $\mathbf{u}$ , must be accordingly computed (reconstructed) in advance at both sides of a given interface out of the cell-centered quantities. The computation of these variables determines the spatial order of the numerical algorithm and, in turn, controls the local jumps at every interface. If these jumps are monotonically reduced the scheme provides more accurate initial guesses for the (either exact or approximate) solution of the local Riemann problems. A wide variety of cell reconstruction procedures is available in the literature. As this issue is particularly relevant for the simulations we report below, we review the most standard choices in the following section.

In addition, our code has the ability of using dif-

ferent approximate Riemann solvers: the Roe solver (Roe 1981), widely employed in classical fluid dynamics simulations, with arithmetically averaged states, the HLLE solver (Harten, Lax & van Leer 1983; Einfeldt 1988) and the Marquina solver (Donat & Marquina 1996), which has been extended to relativistic hydrodynamics by Donat et al (1998). We have performed a detailed comparison of the different solvers finding good overall agreement among them. Hence, for the final computations reported here we have employed Marquina's scheme.

Further specific issues of the hydrodynamical code are in order: 1) the reconstructed (left and right) variables are the physical (primitive) variables  $\mathbf{w}$ , except for the internal energy density,  $\varepsilon$ , as we use a zero-temperature EOS. From these, the remaining (extrapolated) variables are computed algebraically. 2) As we are considering adiabatic evolutions, we only solve for the first four equations of system (15). The internal energy (proportional to the rest-mass density) is obtained algebraically using the EOS. 3) Once all variables have been reconstructed, the set of local Riemann problems (as a result of the discretization on a numerical grid) is solved using Marquina's flux-formula. 4) The numerical fluxes are computed independently for each direction and the time update of the state-vector  $\mathbf{u}$  is done simultaneously using a method of lines in combination with a second-order (in time) conservative Runge-Kutta scheme, as derived by Shu & Osher (1989). 5) After the update of the conserved quantities, the primitive variables must be reevaluated. As the relation between the two sets is not in closed algebraic form, the update of the primitive variables is done using an iterative Newton-Raphson algorithm.

## 4.2 Cell reconstruction procedures

We turn now to describe the different ways we have considered to compute the  $\mathbf{u}^{L,R}$  states at every side of a cell interface. This is commonly referred to as the cell-reconstruction process. In the code we have three basic ways of performing such cell reconstruction.

### 4.2.1 MUSCL

First, we can use a second-order TVD scheme (Harten 1984) of the MUSCL type (Monotonic Upstream Schemes for Conservation Laws, van Leer 1979). The total variation of a given quantity  $\{\mathbf{u}_i^n\}_{i=-\infty}^{\infty}$  on a numerical grid is defined as:

$$TV(\mathbf{u}^n) = \sum_{i=-\infty}^{\infty} |\mathbf{u}_{i+1}^n - \mathbf{u}_i^n|. \quad (28)$$

A 2-level scheme is called TVD if

$$TV(\mathbf{u}^{n+1}) \leq TV(\mathbf{u}^n). \quad (29)$$

The TVD property guarantees the suppression of spurious oscillations near discontinuities.

The code uses slope-limiter methods to construct second-order TVD schemes by means of monotonic piecewise linear reconstructions of the cell-centered quantities. In this scheme,  $\mathbf{u}_i^R$  and  $\mathbf{u}_{i+1}^L$  are computed to second-order accuracy as follows:

$$\mathbf{u}_i^R = \mathbf{u}_i + \sigma_i(x_{i+\frac{1}{2}} - x_i) \quad (30)$$

$$\mathbf{u}_{i+1}^L = \mathbf{u}_{i+1} + \sigma_{i+1}(x_{i+\frac{1}{2}} - x_{i+1}) \quad (31)$$

( $x$  denotes a generic spatial coordinate. In the code it can be either  $r$  or  $\theta$  depending on the direction the integration takes place). Our choice for the slope is the standard minmod slope which provides the desired second-order accuracy for smooth solutions, while still satisfying the TVD property:

$$\sigma_i = \text{minmod} \left( \frac{\mathbf{u}_i - \mathbf{u}_{i-1}}{\Delta x}, \frac{\mathbf{u}_{i+1} - \mathbf{u}_i}{\Delta x} \right), \quad (32)$$

where the minmod function of two arguments is defined by:

$$\text{minmod}(a, b) = \begin{cases} a & \text{if } |a| < |b| \text{ and } ab > 0 \\ b & \text{if } |b| < |a| \text{ and } ab > 0 \\ 0 & \text{if } ab \leq 0 \end{cases}$$

Notice that setting  $\sigma_i = 0$  provides a first-order piecewise constant reconstruction scheme. This is then equivalent to the original scheme by Godunov (1959).

### 4.2.2 ENO

Our second choice involves the use of high-order (up to third-order) ENO schemes (Harten & Osher 1987; Harten et al. 1987). In these schemes, given  $\mathbf{u}_i$ , the cell average of a piecewise smooth function, one must construct a piecewise polynomial function of  $x$  of uniform polynomial degree  $r - 1$ ,  $R(x; \mathbf{u})$ , of the form:

$$R(x; \mathbf{u}) = \sum_{l=1}^{r-1} \frac{1}{l!} b_{i,l} (x - x_i)^l \quad (33)$$

with  $x \in [x_{i-1/2}, x_{i+1/2}]$  and  $b_{i,l}$  being the corresponding polynomial coefficients. This reconstruction polynomial is essentially non-oscillatory in the sense that it satisfies

$$TV(R(x; \mathbf{u}^{n+1})) \leq TV(R(x; \mathbf{u}^n)) + \mathcal{O}(\Delta x^r). \quad (34)$$

This property allows the ENO schemes to maintain the same order of accuracy at local extrema (whereas the TVD schemes always drop to first-order). The left and right states are then given by

$$\mathbf{u}_i^R = R(x_{i+1/2}; \mathbf{u}_i), \quad (35)$$

$$\mathbf{u}_{i+1}^L = R(x_{i+1/2}; \mathbf{u}_{i+1}). \quad (36)$$

The way the coefficients  $b_{i,l}$  are computed for different order reconstruction polynomials is explained in the appendix of Harten et al (1987).

### 4.2.3 PPM

Finally, we also use the third-order Piecewise Parabolic Method (PPM) of Colella & Woodward (1984). In its original design the PPM combined the use of a parabolic reconstruction procedure with Godunov's exact Riemann solver for (Newtonian) ideal gases. Here, we use the reconstruction approach in combination with Marquina's flux formula.

In the PPM scheme the interpolated interface values  $\mathbf{u}_{i+1/2}$  are obtained using the quartic polynomial uniquely determined by the five zone average values  $\mathbf{u}_{i-2}, \dots, \mathbf{u}_{i+2}$  in the following way:

$$\begin{aligned} \mathbf{u}_{i+1/2} &= \mathbf{u}_i + \frac{\Delta x_i}{\Delta x_i + \Delta x_{i+1}} (\mathbf{u}_{i+1} - \mathbf{u}_i) \\ &+ \frac{1}{\sum_{j=-1}^2 \Delta x_{i+j}} \\ &\times \left\{ \frac{2\Delta x_{i+1} + \Delta x_i}{\Delta x_i + \Delta x_{i+1}} \mathbf{X} (\mathbf{u}_{i+1} - \mathbf{u}_i) \right. \\ &- \frac{\Delta x_{i-1} + \Delta x_i}{2\Delta x_i + \Delta x_{i+1}} \Delta x_i \delta_m \mathbf{u}_{i+1} \\ &\left. + \frac{\Delta x_{i+1} + \Delta x_{i+2}}{\Delta x_i + 2\Delta x_{i+1}} \Delta x_{i+1} \delta_m \mathbf{u}_i \right\}, \end{aligned} \quad (37)$$

with

$$\mathbf{X} = \frac{\Delta x_{i-1} + \Delta x_i}{2\Delta x_i + \Delta x_{i+1}} - \frac{\Delta x_{i+2} + \Delta x_{i+1}}{2\Delta x_{i+1} + \Delta x_i}, \quad (38)$$

and  $\delta_m \mathbf{u}_i = \min(|\delta \mathbf{u}_i|, 2|\mathbf{u}_i - \mathbf{u}_{i-1}|, 2|\mathbf{u}_{i+1} - \mathbf{u}_i|) \times \text{sign}(\delta \mathbf{u}_i)$  if  $(\mathbf{u}_{i+1} - \mathbf{u}_i)(\mathbf{u}_i - \mathbf{u}_{i-1}) > 0$  and 0 otherwise. Additionally

$$\begin{aligned} \delta \mathbf{u}_i &= \frac{\Delta x_i}{\Delta x_{i-1} + \Delta x_i + \Delta x_{i+1}} \\ &\times \left[ \frac{2\Delta x_{i-1} + \Delta x_i}{\Delta x_{i+1} + \Delta x_i} (\mathbf{u}_{i+1} - \mathbf{u}_i) \right. \\ &\left. + \frac{\Delta x_i + 2\Delta x_{i+1}}{\Delta x_{i-1} + \Delta x_i} (\mathbf{u}_i - \mathbf{u}_{i-1}) \right]. \end{aligned} \quad (39)$$

This algorithm provides a third-order accurate representation of  $\mathbf{u}_{i+1/2}$ . For smooth flow solutions the left and right values are then given by:

$$\mathbf{u}_{i+1}^L = \mathbf{u}_i^R = \mathbf{u}_{i+\frac{1}{2}}. \quad (40)$$

In the presence of discontinuities these values are modified to ensure the monotone character of the interpolation parabola. Colella and Woodward (1984) proposed the following modifications:  $\mathbf{u}_i^L = \mathbf{u}_i^R = \mathbf{u}_i$  if  $(\mathbf{u}_i^r - \mathbf{u}_i)(\mathbf{u}_i - \mathbf{u}_i^l) \leq 0$ ,  $\mathbf{u}_i^L = 3\mathbf{u}_i - 2\mathbf{u}_i^R$  if  $(\mathbf{u}_i^r - \mathbf{u}_i^l)(\mathbf{u}_i - 0.5(\mathbf{u}_i^L + \mathbf{u}_i^R)) > (\mathbf{u}_i^r - \mathbf{u}_i^l)^2/6$  and  $\mathbf{u}_i^R = 3\mathbf{u}_i - 2\mathbf{u}_i^L$  if  $-(\mathbf{u}_i^r - \mathbf{u}_i^l)(\mathbf{u}_i - 0.5(\mathbf{u}_i^L + \mathbf{u}_i^R)) > (\mathbf{u}_i^r - \mathbf{u}_i^l)^2/6$ .

Additionally, the PPM scheme incorporates a special treatment of contact discontinuities (contact steepening) as well as a "flattening" procedure to avoid spurious post shock oscillations. Details on these more spe-

cialized aspects of the PPM scheme can be found in the original reference of Colella & Woodward (1984).

### 4.3 Marquina's flux formula

The way the numerical flux at a given interface separating the states  $\mathbf{u}^L$  and  $\mathbf{u}^R$  is computed in Marquina's solver, is as follows: We first compute the sided local characteristic variables and fluxes

$$\begin{aligned} \omega_L^p &= \mathbf{I}^p(\mathbf{u}_L) \cdot \mathbf{u}_L & \phi_L^p &= \mathbf{I}^p(\mathbf{u}_L) \cdot \mathbf{f}(\mathbf{u}_L), \\ \omega_R^p &= \mathbf{I}^p(\mathbf{u}_R) \cdot \mathbf{u}_R & \phi_R^p &= \mathbf{I}^p(\mathbf{u}_R) \cdot \mathbf{f}(\mathbf{u}_R), \end{aligned}$$

for  $p = 1, \dots, 5$ . Here  $\mathbf{I}^p(\mathbf{u}_L)$ ,  $\mathbf{I}^p(\mathbf{u}_R)$ , are the (normalized) left eigenvectors of the Jacobian matrices of the system. Let  $\lambda_1(\mathbf{u}_L), \dots, \lambda_5(\mathbf{u}_L)$  and  $\lambda_1(\mathbf{u}_R), \dots, \lambda_5(\mathbf{u}_R)$  be their corresponding eigenvalues. For  $k = 1, \dots, 5$  the procedure is the following:

- If  $\lambda_k(\mathbf{u})$  does not change sign in  $[\mathbf{u}_L, \mathbf{u}_R]$ , then the scalar scheme is upwind

If  $\lambda_k(\mathbf{u}_L) > 0$  then

$$\begin{aligned} \phi_+^k &= \phi_L^k, \\ \phi_-^k &= 0, \end{aligned}$$

else

$$\begin{aligned} \phi_+^k &= 0, \\ \phi_-^k &= \phi_R^k, \end{aligned}$$

endif

- Otherwise, the scalar scheme is switched to the more viscous, entropy-satisfying, local-Lax-Friedrichs scheme

$$\alpha_k = \max_{\mathbf{u} \in \Gamma(\mathbf{u}_L, \mathbf{u}_R)} |\lambda_k(\mathbf{u})|,$$

$$\begin{aligned} \phi_+^k &= .5(\phi_L^k + \alpha_k \omega_L^k), \\ \phi_-^k &= .5(\phi_R^k - \alpha_k \omega_R^k), \end{aligned}$$

$\Gamma(\mathbf{u}_L, \mathbf{u}_R)$  is a curve in phase space connecting  $\mathbf{u}_L$  and  $\mathbf{u}_R$ . In addition,  $\alpha_k$  can be determined as

$$\alpha_k = \max\{|\lambda_k(\mathbf{u}_L)|, |\lambda_k(\mathbf{u}_R)|\}.$$

Marquina's flux formula is then:

$$\hat{\mathbf{f}}_{i+1/2} = \sum_{p=1}^5 (\phi_+^p \mathbf{r}^p(\mathbf{u}_L) + \phi_-^p \mathbf{r}^p(\mathbf{u}_R)), \quad (41)$$

where  $\mathbf{r}^p(\mathbf{u}_L)$ ,  $\mathbf{r}^p(\mathbf{u}_R)$ , are the right (normalized) eigenvectors of the system. For further details on this solver we refer the reader to Donat & Marquina (1996).

### 4.4 Numerical grid and boundary conditions

The code uses spherical polar coordinates  $(r, \theta, \phi)$  and assumes axisymmetry, i.e., there are no  $\phi$  derivatives. The computational domain in the radial direction extends from 0 to 1.2 times the radius of the star. In

the polar direction the domain extends from 0 (pole) to  $\pi/2$  (equator). For the study of radial pulsations of spherical stars we use fine grids of, typically, 400 radial grid-points and only one angular grid-point. For nonradial pulsations, for which the  $\theta$ -velocity does not vanish, the typical grid-sizes we use are  $80^2$  to  $120^2$ . For studying quasi-radial pulsations in rotating stars, we typically use more points in the radial direction than in the angular direction.

We use a number of boundary grid-zones which depends on the stencil size of the different schemes. Hence, for the MUSCL and ENO2 schemes, we need to impose boundary conditions in two additional zones at each end of the domain. For the ENO3 and PPM schemes, the number of additional zones is four. The boundary conditions are applied to  $\rho_0, v_r, v_\theta$  and  $v_\phi$  and they are as follows: at the center ( $r = 0$ ) the radial fluxes vanish. Hence, the radial velocity is anti-symmetric across the origin. The remaining variables are symmetric. At the outer radial boundary, the “atmosphere” is re-set to the initial data after each time step. At the pole ( $\theta = 0$ ) and equator ( $\theta = \pi/2$ ), all variables are symmetric, except for  $v_\theta$ , since the initial data have equatorial-plane symmetry and, in this paper, we assume that  $v_\theta$  is a sum of “polar” (even) vector harmonics.

## 5 CODE TESTS

### 5.1 Shock tube test

We begin by testing the behaviour of the code and of its different schemes in a standard shock tube problem in flat spacetime. Although this is a known test and the results are, to some extent, well documented in the literature (see, e.g., Donat et al 1998, Martí and Müller 1996) our motivation to include them here is to show the correct implementation of the different schemes in the present code, by comparing to a non trivial exact solution with all types of nonlinear waves: a shock, a contact discontinuity and a rarefaction wave.

Results for the shock tube test are plotted in Fig 1. The initial discontinuous conditions correspond to problem 1 in Martí and Müller (1996). The different panels show the final state, at  $t = 0.4$ , for the velocity, density and pressure for all numerical schemes. The solid lines represent the exact solution and the symbols indicate the numerical solution. We use a grid of 200 zones spanning a domain of unit length. The density and pressure are scaled by a factor of 10 and 20 respectively. From this figure, we conclude that the implementation of all schemes is correct as all of them reproduce the exact solution and give the correct wave speeds. The higher order methods such as ENO3 and PPM give, as expected, the best results.

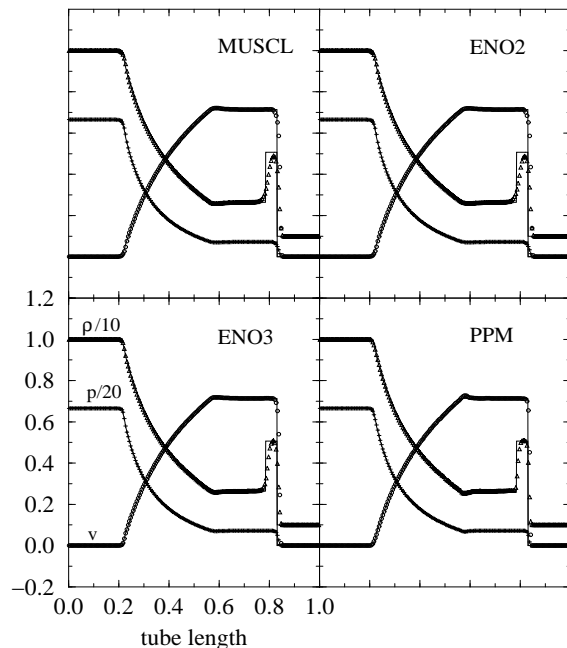


**Figure 1.** Results for the shock tube test for the different implemented numerical schemes. The solid lines indicate the exact solution, at  $t = 0.4$ . The symbols indicate the numerical solution for the velocity (circles), density (triangles) and pressure (plus signs). The density and pressure are scaled by a factor of 10 and 20 respectively.

### 5.2 Spherical stars

Next, we test our code in the non-rotating limit. We study the hydrodynamical evolution of non-rotating neutron star models in stable equilibrium. Since our axisymmetric code uses spherical polar coordinates, it can also be run in essentially 1-D, by using only one grid point in the angular direction. We determine radial pulsation frequencies and compare to frequencies expected from perturbation theory. In 2-D, we study non-rotating stars that are perturbed from equilibrium by an axisymmetric quadrupole perturbation and also compare the pulsation frequencies to the ones obtained with a perturbative code.

We will focus our attention on two representative neutron star models: Model 1 is a  $N = 1.5$  relativistic soft polytrope with  $M/R = 0.056$ , while model 2 is a more relativistic and stiffer polytrope with  $M/R = 0.15$ . Table 1 lists the polytropic index  $N$ , polytropic constant  $K$ , central density  $\rho_c$ , mass  $M$  and circumferential radius  $R$  for the two models considered (all quantities are dimensionless, using  $c = G = M_\odot = 1$ ).

### Initial models of spherical stars

	$N$	$K$	$\rho_c$	$M$	$R$
Model 1	1.5	4.349	$8.10 \times 10^{-4}$	0.57	10.11
Model 2	1.0	100	$1.28 \times 10^{-3}$	1.40	9.59

**Table 1.** Dimensionless ( $c = G = M_\odot = 1$ ) equilibrium properties of the two representative spherical neutron star models.

#### 5.2.1 1-D evolutions: radial pulsations

The numerical evolution of initially static, non-rotating stars is influenced by the size and sign of the truncation errors of the hydrodynamical scheme. We observe the following characteristics, when using HRSC schemes:

- (i) The truncation errors at the surface of the star initiate small-amplitude radial pulsations.
- (ii) The radial pulsations are dominated by a set of discrete frequencies, which correspond to the normal modes of pulsation of the star.
- (iii) The numerical viscosity of the finite-difference scheme damps the pulsations and the damping is stronger for the higher frequency modes.
- (iv) The presence of a constant-density atmosphere affects the finite differencing at the surface grid-cells, which increases the numerical damping of pulsations and also can cause the star to drift to larger densities.

Thus, we find that any hydrodynamical evolution of neutron star models, with the present HRSC schemes, will be accompanied by small-amplitude radial (or quasi-radial for rotating stars) pulsations. The initial amplitude of the radial pulsations and the small drift in density converge to zero at the expected order rate, with increasing resolution. The value of the density in the atmosphere region can have a large effect on the damping of the pulsations, if it is too large. To minimize this effect, we typically set the density of the atmosphere equal to  $10^{-6}$  times the density of the central density of the star.

Fig. 2 shows the evolution of the radial velocity  $v_r$  at a radius of  $0.25R$ , with Model 1 as initial model. We use the second-order MUSCL scheme with 400 radial grid-points. The radial velocity is initially a very complex function of time. As we will show next, the pulsation consists mainly of a superposition of normal modes of oscillation of the fluid. The high frequency normal modes are damped quickly and after 20ms the star pulsates mostly in its lowest frequency modes. Because these oscillations are initiated by the truncation errors, the magnitude of the radial velocity is extremely small. The velocity oscillates around a non-zero resid-

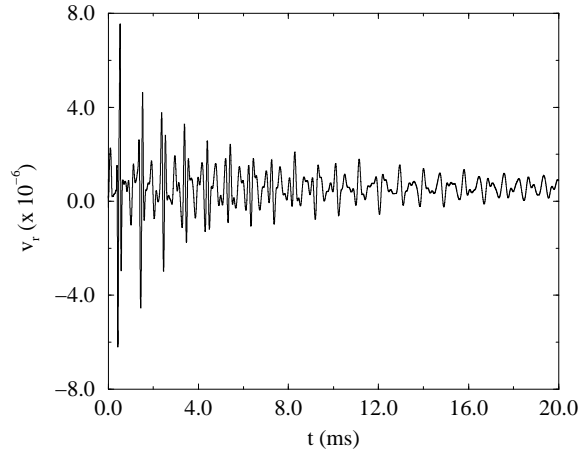


**Figure 2.** Time evolution of the radial velocity of a spherical star (model 1). The radial pulsations are initiated by the truncation errors of the finite-difference scheme and are mainly a superposition of normal modes of the star.

ual, which also converges to zero as second order with increasing resolution.

The small-amplitude radial pulsations in the non-linear, fixed spacetime evolutions correspond to linear normal modes of pulsation in the relativistic Cowling approximation (McDermott, Van Horn & Scoll 1983), in which perturbations of the spacetime are ignored. A Fourier transform of the density or radial velocity evolution can be used to compute the normal mode frequencies. Fig. 3 shows the Fourier transform of the radial-velocity evolution shown in Fig. 2. The normal mode frequencies stand out as sharp peaks on a continuous background. The width of the peaks increases with frequency. The frequencies of radial pulsations identified from Fig. 3 are shown in Table 2.

To compare the obtained frequencies to linear normal mode frequencies, we use a code that solves the linearized relativistic pulsation equations for the stellar fluid in the Cowling approximation, as an eigenvalue problem. In Table 2 we present the results of this comparison. The typical agreement between frequencies computed by the two methods is better than 0.5% for the fundamental  $F$ -mode and the lowest frequency harmonics  $H_1 - H_4$  and better than 0.8% for the higher harmonics  $H_5 - H_9$ . We note that these frequencies are global, as they should be for normal mode pulsations, i.e. the frequencies are the same at any point in the star, in both the radial velocity and density evolution. This is a strong test for the accuracy of the evolution code and our results can be used as a testbed computation for other relativistic multi-dimensional evolution codes.

While all four schemes give essentially the same radial pulsation frequencies there are some differences



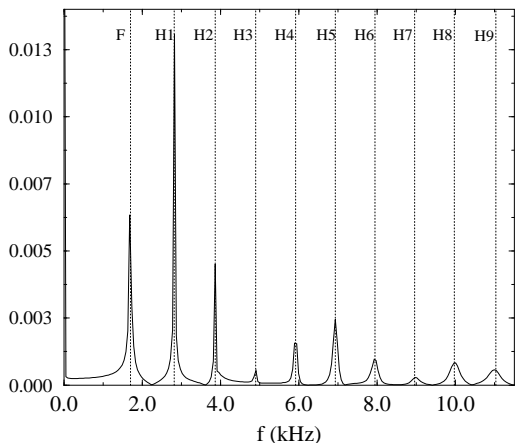


**Figure 3.** Fourier transform of the evolution of the radial velocity in Fig. 2. The frequencies are in excellent agreement with linear normal mode frequencies computed with an eigenvalue code (vertical dotted lines). The units of the vertical axis are arbitrary.

### Radial Pulsation Frequencies. Model 1

Mode	nonlinear (kHz)	Cowling (kHz)	difference
$F$	1.703	1.697	0.3%
$H_1$	2.820	2.807	0.5%
$H_2$	3.862	3.868	0.02%
$H_3$	4.900	4.910	0.2%
$H_4$	5.917	5.944	0.4%
$H_5$	6.930	6.973	0.6%
$H_6$	7.947	8.001	0.7%
$H_7$	8.960	9.029	0.8%
$H_8$	9.973	10.057	0.8%
$H_9$	11.030	11.086	0.5%

**Table 2.** Comparison of small-amplitude radial pulsation frequencies obtained with the present nonlinear evolution code to linear perturbation mode frequencies in the relativistic Cowling approximation. The equilibrium model is a non-rotating  $N = 1.5$  relativistic polytrope with  $M/R = 0.056$ .

in the hydrodynamical evolution that are worth to be emphasized. Fig. 4 shows the density evolution, at  $R/2$ , for Model 2, using all four different numerical schemes. The most striking difference is that the secular drift in the density is much smaller for the third-order PPM and ENO3 schemes than for the second-order MUSCL and ENO2 schemes. With a resolution of 400 radial points, the drift is extremely small: after 10ms the den-

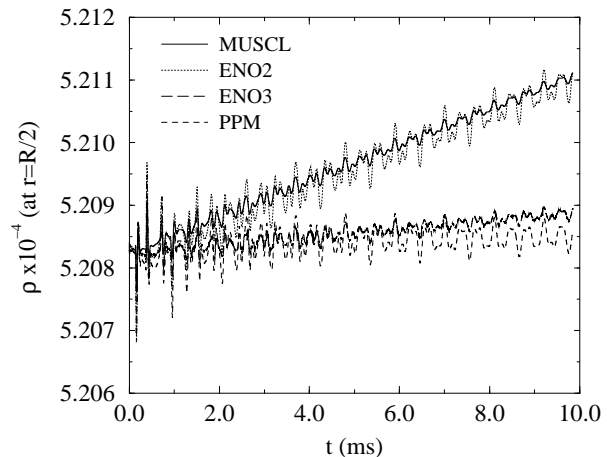


**Figure 4.** Time evolution of the density at half-radius, initiated by truncation errors, for a non-rotating initial model (model 2). The small secular drift in density, when using second order schemes (MUSCL and ENO2), is significantly reduced or nearly eliminated, using third order schemes (ENO3 and PPM).

sity has increased by only 0.3%. With the third-order schemes, ENO3 and PPM, this drift is considerably smaller, being practically unnoticeable in the case of PPM. Another difference among the schemes, is that each one of them excites the various normal modes of pulsation with different amplitude in each mode. In ENO3, the truncation errors at the surface also excite some very high-frequency oscillations, in addition to low-order normal modes. These high-frequency oscillations, however, do not represent a problem in the identification of normal modes in a Fourier transform. Finally, the numerical damping rate of the excited pulsations is similar in the four schemes, with ENO2 and PPM showing the smallest damping rate.

### 5.2.2 2-D evolutions: quadrupole pulsations

Like radial pulsations, small-amplitude nonradial pulsations can be studied with the present evolution code and the obtained frequencies can be compared to perturbation results. We find that the truncation errors of the finite difference scheme do not excite nonradial oscillations with amplitudes large enough that one can identify them accurately in an evolution of unperturbed initial configurations. Instead, one has to perturb the static initial configuration, using an appropriate eigenfunction for each nonradial angular index  $l$ . For example, to excite the lowest-order quadrupolar ( $l = 2$ ) pulsations in a spherical star, we perturb the  $v_\theta$  velocity component, using an approximate eigenfunction with angular behaviour same as the spherical harmonic function  $Y_2^0$  and a simple  $\sin(\pi r/R)$  radial behaviour.

**Quadrupole Pulsation Frequencies. Model 2**

Mode	nonlinear (kHz)	Cowling (kHz)	difference
$f$	1.852	1.8843	1.7%
$p_1$	4.095	4.1099	0.4%
$p_2$	6.009	6.0351	0.4%
$p_3$	7.858	7.8733	0.2%
$p_4$	9.683	9.6740	0.1%

**Table 3.** Comparison of small-amplitude quadrupole ( $l = 2$ ) pulsation frequencies, obtained with the present nonlinear evolution code, to linear perturbation mode-frequencies in the relativistic Cowling approximation. The equilibrium model is a nonrotating  $N = 1.0$  relativistic polytrope with  $M/R = 0.15$  (Model 2).

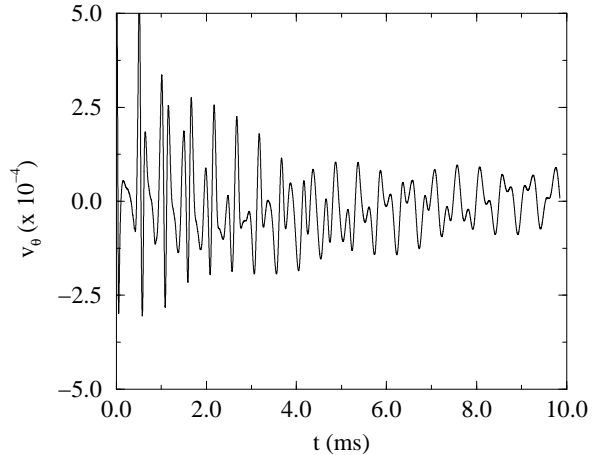
The frequencies of the nonradial modes can then be identified in a Fourier transform of the time-evolution of the  $v_\theta$  velocity component.

Table 3 shows a similar comparison, as in Table 2, for the quadrupole ( $l = 2$ ) pulsations of model 2. Since the nonradial modes have to be computed on a two-dimensional grid, we cannot use resolutions as high as in the 1-D computations. For a grid-size of  $120 \times 60$  zones, the difference between frequencies computed by the two methods is 1.7% for the fundamental  $f$ -mode and better than 0.4% for the  $p$ -modes  $p_1 - p_4$ . For this grid-size, frequencies higher than the  $p_4$  mode could not be computed accurately, because the grid is too coarse to resolve their eigenfunctions (higher harmonic eigenfunctions have a larger number of nodes in the radial direction).

Fig. 5 shows the evolution of the  $v_\theta$  at a radial distance of  $0.25R$ , for model 2, perturbed with an approximate quadrupolar eigenfunction of small amplitude. In this evolution, the PPM scheme was used with an  $(r, \theta)$ -grid of  $120 \times 60$  points. The evolution is mainly a sum of the lowest-order quadrupolar pulsation modes of the star and allows for the accurate identification of the  $l = 2$  normal-mode frequencies.

### 5.3 Rotating stars

We now turn to the evolution of initially stationary, uniformly rotating neutron stars. In the rotating case, we focus on a rapidly rotating model, with angular velocity equal to 92% of the mass-shedding (Kepler) limit and equation of state and central density parameters same as model 2 in Table 1. In these evolutions, we observe the same qualitative properties as for non-rotating stars and an additional important property: *the rotation law (angular-momentum distri-*



**Figure 5.** Time evolution of the  $v_\theta$  velocity component at  $0.25R$ , for a perturbed nonrotating initial model (Model 2) using the PPM scheme and an  $(r, \theta)$ -grid of  $120 \times 60$  points. The evolution is mainly a sum of the lowest-order quadrupolar pulsation modes of the star, excited using an approximate low-amplitude eigenfunction.

*bution*), changes near the stellar surface, due to the truncation errors of the finite difference scheme. This can be attributed to mainly two reasons: (i) the velocity component  $v_\phi$  of the fluid has a maximum at the surface and the second-order TVD scheme, for example, although high-order accurate in smooth regions of the solution, reduces to only first-order at extrema of the reconstructed variables. ENO schemes, on the other hand, retain the order at local extrema. However, as we show below, preserving the angular momentum distribution near the surface of the star, is still problematic with such schemes. This points to a second reason, for this behaviour. (ii) The code evolves the relativistic momenta ( $S_i$ ) and the velocity components (as well as the other “primitive” variables) must be recovered through a root-finding procedure, which involves dividing by the density (see Martí & Müller (1996) for details of this procedure). At the surface of the star (where the density is very small) this contributes to obtaining less than second-order accuracy.

A typical example of the evolution of a rotating star is presented in Fig. 6, which shows the evolution of the velocity component  $v_\phi$  obtained with the four schemes and with a grid-size of  $160 \times 40$  zones in  $r$  and  $\theta$  respectively. Depicted is the initial equilibrium solution (solid line) as a function of the radial coordinate (in the equatorial plane) and the final configuration, after an evolution time of  $5ms$ , which corresponds to 4 rotational periods. The figure shows that  $v_\phi$  remains close to its initial value in the interior of the star. But, near the surface,  $v_\phi$  decreases with time. It is evident from this figure that there are significant differences be-

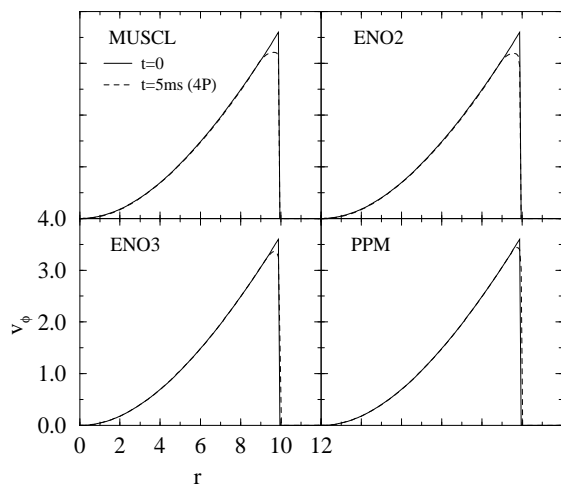


**Figure 6.** Evolution of the velocity component  $v_\phi$  of a rotating star. The profiles show the radial dependence in the equatorial plane ( $\theta = \pi/2$ ). Dimensionless units are used in both axes.

tween second-order (top panels) and third-order (lower panel) schemes. For the same resolution, the third-order schemes result in a more accurate preservation of the initial rotation law, both in the interior and the surface of the star. We note that, in the interior, all schemes give satisfactory results, but for the third-order schemes, the difference between the initial and final solution is negligible. The more accurate preservation of the rotation law for the third order schemes is emphasized in Fig. 7, which shows the change in  $v_\phi$  at the interior ( $r = 6$ , top panel) and at the surface of the star ( $r = 9.8$ , bottom panel), as a function of time, for the four difference schemes. The values depicted correspond to the equatorial plane of the star ( $\theta = \pi/2$ ). At the interior, the third-order schemes (ENO3 and PPM) retain accurately the initial rotation law (PPM shows a tiny initial jump to a slightly lowest value), while the second-order schemes (ENO2 and MUSCL) show a very small secular drift (0.8% after 5ms) accompanied by oscillations. Correspondingly, at the surface, bottom panel of Fig. 7, all schemes show a nearly linear change in  $v_\phi$ , with the third-order PPM scheme having the smallest slope.

In Fig. 8 we show the momentum component  $S_\phi$  of the same rotating star for the four numerical schemes as in Fig. 6. This is one of the conserved quantities  $\mathbf{u}$  directly evolved with the code. As mentioned previously, the recovery of the primitive variables is done via a root-finding procedure which involves dividing by the density. Both quantities,  $S_\phi$  and  $\rho$ , are very close to zero around the surface layer and hence the procedure is very sensitive to truncation errors. Whereas the four schemes give accurate results for the evolution of  $S_\phi$ , the computation of  $v_\phi$  near the surface of the star is

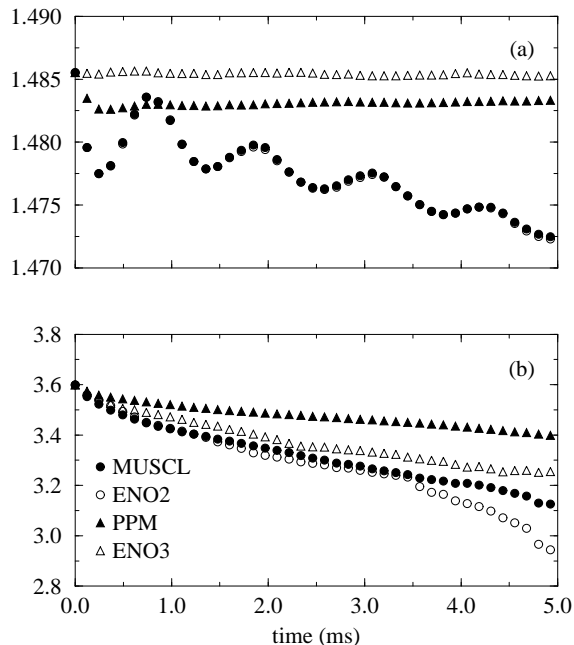


**Figure 7.** Evolution of  $v_\phi$  at two different radii of a rotating star, for the four different schemes: (a)  $r = 6$  (interior), (b)  $r = 9.8$  (surface). The values are measured in the equatorial plane ( $\theta = \pi/2$ ). In the interior of the star the third-order schemes (ENO3 and PPM) retain accurately the initial values while the second-order schemes (ENO2 and MUSCL) show a very small secular drift (0.8% after 5ms) accompanied by oscillations. This drift is due to finite-differencing truncation errors. Both second-order schemes behave almost identically. Near the surface,  $r = 9.8$  (bottom panel), the drift is more pronounced, being smallest for the third-order PPM scheme.

only first-order accurate irrespective of the numerical method.

We plot in Fig. 9 the initial and final configurations of the azimuthal component of the velocity as a function of the angular coordinate,  $\theta$ , at half the radius of the star. The solid line represents the initial solution and the dashed line corresponds, again, to a final solution after 5ms (four rotational periods). All schemes give excellent accurate results, most notably ENO3 and PPM.

Quasi-radial pulsations of rotating relativistic stars have only been studied in the slow-rotation limit (but without the assumption of a fixed spacetime) by Hartle & Friedman (1975) (see also Datta et al. 1998). We can study such pulsations for rapidly rotating neutron stars, using appropriate radial eigenfunctions to excite them. In Fig. 10 we show the time evolution of the velocity (in the equatorial plane) at  $0.25R$ , after an initial small-amplitude radial excitation of the stationary star studied in this section. The quasi-radial pulsations can be followed accurately for many dynamical times.

We note that the computation of modes in a ro-

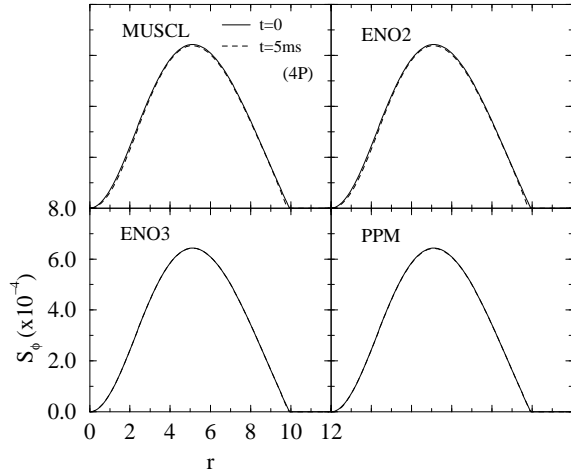


**Figure 8.** Evolution of the momentum component  $S_\phi$  of a rotating star. The profiles show the radial dependence in the equatorial plane ( $\theta = \pi/2$ ). Dimensionless units are used in both axes.

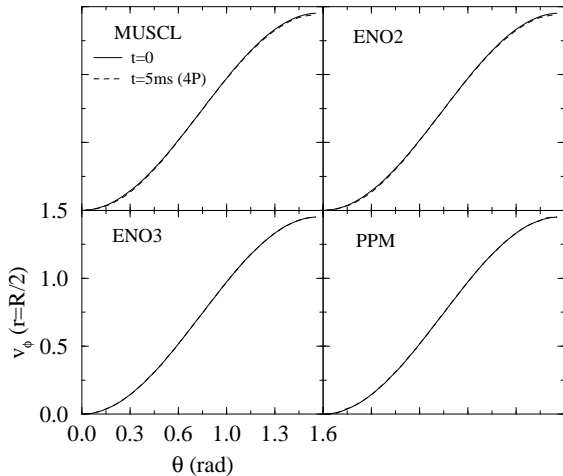


**Figure 9.** Evolution of the velocity component  $s_\phi$  of a rotating star. The profiles show the angular dependence at half the radius of the star.

tating star requires an appropriate excitation, even for quasi-radial modes, in order to obtain the corresponding frequencies with good accuracy in a Fourier transform of hydrodynamical variables. A detailed study of quasi-radial modes in rapidly rotating relativistic stars of various equations of state and rotation laws (in the Cowling approximation), will appear elsewhere.

## 6 DISCUSSION

We have developed a numerical code which integrates the equations of general relativistic hydrodynamics to study pulsations of rapidly-rotating relativistic stars

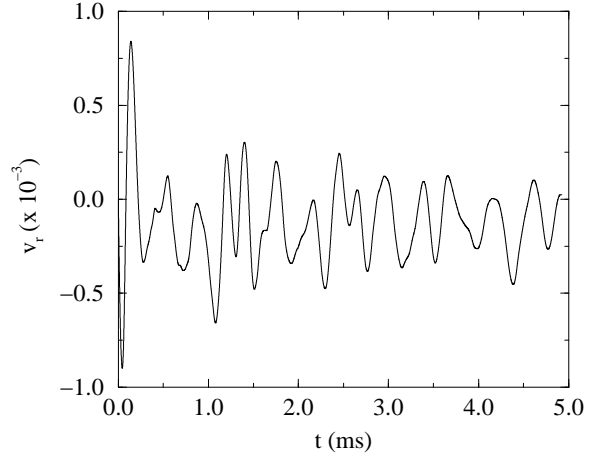


**Figure 10.** Evolution of the radial velocity at  $0.25R$  for a rotating initial model (Model 2) using the PPM scheme and a  $(r, \theta)$ -grid of  $160 \times 40$  points. This figure shows the quasi-radial pulsations of the star as a result of a external perturbation.

in a fixed background spacetime. The finite-difference code is based on a state-of-the-art approximate Riemann solver (Donat & Marquina 1996). Our axisymmetric relativistic hydrodynamical code is capable of accurately evolving rapidly rotating stars for many rotational periods. We find that, for non-rotating stars, small amplitude oscillations have frequencies that agree with linear, radial and nonradial, normal mode frequencies in the Cowling approximation. This study has been performed using a representative set of second- and third-order TVD and ENO numerical schemes.

Modern HRSC numerical schemes (as the ones used in our code), satisfying the “total variation diminishing” property (Harten 1984), are second-order accurate in smooth regions of the flow, but only first-order accurate at local extrema. In our rotating star evolutions we find that this results in a secular drift of the angular momentum distribution near the surface of the star. Essentially non-oscillatory schemes (Harten & Osher 1987), which retain the order at local extrema, were also used to investigate the preservation of the initial rotation law near the surface, with results similar to the second-order TVD methods. The first-order accuracy obtained at the surface layer irrespective of the method employed pointed out to the ill-posedness of the primitive variables recovery procedure as the reason of the angular momentum loss. The numerical scheme which has the smallest change in the rotation law after many rotation periods is the third-order PPM scheme.

It would be interesting to investigate if the computational cost of the present code can be reduced with the use of surface-adapted coordinates or fixed-mesh refinement and also to analyze whether the change of

the rotation law per rotation period will be significantly smaller in a frame co-rotating with the star.

The numerical findings reported in this paper are important for the study of small-amplitude and non-linear oscillations of rotating neutron stars such as  $f$ ,  $p$  and  $r$ -modes oscillations.

Having adopted the PPM third-order scheme as our preferred choice for studying hydrodynamical pulsations of rapidly-rotating stars, we plan to investigate axisymmetric pulsations of rotating proto-neutron stars, allowing for various rotation laws and equations of state.

### ACKNOWLEDGEMENTS

We thank José M. Ibáñez, Bernard F. Schutz and Ed Seidel for helpful discussions, and John L. Friedman and Philippos Papadopoulos for helpful comments on the manuscript. J.A.F acknowledges financial support from a TMR grant from the European Union (contract nr. ERBFMBICT971902). He also wants to thank Rosa Donat for useful discussions on numerical schemes and for allowing us to use her ENO cell-reconstruction routines. K.D.K. is grateful to the Max-Planck-Institut für Gravitationsphysik (Albert-Einstein-Institut), Golm, for generous hospitality.

### REFERENCES

N. Andersson, *ApJ* **502**, 708 (1998).  
 N. Andersson, K.D. Kokkotas & B.F. Schutz, *ApJ* **510**, 846 (1999).  
 F. Banyuls, J.A. Font, J.M<sup>a</sup>. Ibáñez, J.M<sup>a</sup>. Martí & J.A. Miralles, *ApJ* **476**, 221 (1997).  
 T.W. Baumgarte, S.A. Hughes & S.L. Shapiro, preprint (1999) (gr-qc/9902024)  
 E. M. Butterworth & J.R. Ipser, *ApJ* **204**, 200 (1976)  
 S. Chandrasekhar, *Phys. Rev. Lett.* **24**, 611 (1970).  
 G.B. Cook, S.L. Shapiro & S.A. Teukolsky, *ApJ* **398**, 203 (1992).  
 P. Colella & P.R. Woodward, *J. Comp. Phys.* **54**, 174 (1984).  
 B. Datta, S.S. Hasan, P.K. Sahu, A.R. Prasanna, *International J. of Modern Physics D*, Vol. 7, No. 1 49 (1998).  
 R. Donat & A. Marquina, *J. Comput. Phys.* **125**, 42 (1996).  
 R. Donat, J.A. Font, J.M<sup>a</sup>. Ibáñez & A. Marquina, *J. Comput. Phys.* **146**, 58 (1998).  
 J.A. Font, M. Miller, W.-M. Suen, & M. Tobias, *Phys. Rev. D*, in press (1999) (gr-qc/9811015).  
 J.L. Friedman & B.F. Schutz, *ApJ* **222**, 281 (1978).  
 J.L. Friedman & S.M. Morsink, *ApJ* **502**, 714 (1998).  
 J.L. Friedman (1999) private communication.  
 E.ourgoulhon, *A&A* **252**, 651 (1991).  
 A. Harten, *SIAM J. Numer. Anal.* **21**, 1 (1984).  
 A. Harten & S. Osher, *SIAM J. Numer. Anal.* **24**, 279 (1987).  
 A. Harten, B. Engquist, S. Osher & S.R. Chakrabarthy, *J. Comp. Phys.* **71**, 231 (1987).  
 J.B. Hartle & J.L. Friedman, *ApJ* **196**, 653 (1975).

J.L. Houser, J.M. Centrella & S.C. Smith, *Phys. Rev. Lett.* **72**, 1314 (1994).  
 J.M<sup>a</sup>. Ibáñez (1998) private communication.  
 J.M<sup>a</sup>. Ibáñez & J.M<sup>a</sup>. Martí, *J. Comput. Appl. Math.*, in press (1999).  
 H. Komatsu, Y. Eriguchi & I. Hachisu, *MNRAS* **237**, 355 (1989).  
 L. Lindblom, B.J. Owen & S.M. Morsink, *Phys. Rev. Lett.* **80**, 4843 (1998).  
 A. Marquina, *SIAM J. Scient. Stat. Comp.* **15**, 892 (1994).  
 G.J. Mathews, P. Marronetti & J.R. Wilson, *Phys. Rev. D.* **58**, 043003 (1998).  
 J.M<sup>a</sup>. Martí, J.M<sup>a</sup>. Ibáñez & J.A. Miralles, *Phys. Rev. D* **43**, 3794 (1991).  
 J.M<sup>a</sup>. Martí & E. Müller, *J. Comput. Phys.* **123**, 1 (1996).  
 P.N. McDermott, H.M. Van Horn & J.F. Scholl, *ApJ* **268**, 837 (1983).  
 M. Miller, W.-M. Suen & M. Tobias, preprint (1999) (gr-qc/9904041)  
 T. Nakamura & K. Oohara, talk at Numerical Astrophysics (1998) (gr-qc/9812054).  
 D.W. Neilsen & M.W. Choptuik, preprint (1999) (gr-qc/9904052)  
 T. Nozawa, N. Stergioulas, E.ourgoulhon & Y. Eriguchi, *Astr. Ap. Supp. Ser.* **132**, 431 (1998).  
 B.J. Owen, L. Lindblom, C. Cutler, B. F. Schutz, A. Vecchio & N. Andersson, *Phys. Rev. D* **58**, 084020 (1998).  
 P. Papadopoulos & J.A. Font, *Phys. Rev. D*, in press (1999) (gr-qc/9902018).  
 L. Rezzolla, F.K. Lamb and S.L. Shapiro, preprint (1999).  
 P.L. Roe, *J. Comput. Phys.* **43**, 357 (1981).  
 J.V. Romero, J.M<sup>a</sup>. Ibáñez, J.M<sup>a</sup>. Martí & J.A. Miralles, *ApJ* **462**, 836 (1996).  
 M. Shibata, preprint (1999a), (gr-qc/9905058).  
 M. Shibata, preprint (1999b).  
 C.-W. Shu & S. Osher, *J. Comput. Phys.* **83**, 32 (1989).  
 H.C. Spruit, *A&A* **341**, L1 (1999).  
 N. Stergioulas & J.L. Friedman, *ApJ* **444**, 306 (1995).  
 N. Stergioulas, *Living Reviews in Relativity*, **1998-8** (1998) (<http://www.livingreviews.org/Articles/Volume1/1998-8stergio/>).  
 N. Stergioulas, J.A. Font & K.D. Kokkotas, Proceedings of the 19th Texas Symposium on Relativistic Astrophysics, in press (1999) (gr-qc/9904009).